Modeling and Predicting Land Use Land Cover Spatiotemporal Changes: A Case Study in Chalus Watershed, Iran

Sepideh Jalayer, Alireza Sharifi, Dariush Abbasi-Moghadam, Aqil Tariq, and Shujing Qin

***Abstract*—Land use and land cover (LULC) change is a main driver of global environmental change and has destructive effects on the structure and function of the ecosystem. This study attempts to detect temporal and spatial changes in LULC patterns of the Chalus watershed during the last two decades using multitemporal Landsat images and predict the future LULC changes and patterns of the Chalus watershed for the year 2040. A hybrid method between segment-based and pixel-based classification was applied for each Landsat image in 2001, 2014, and 2021 to produce LULC maps of the Chalus watershed. In this study, the transition potential maps and the transition probability matrices between LULC types were provided by the support vector machine algorithm and the Markov chain model, respectively, to project the 2021 and 2040 LULC maps. The achieved K-index values that compared the simulated LULC map with the actual LULC map of the year 2021 resulted in a Kstandard = 0.9160, Kno = 0.9379, Klocation = 0.9318, and KlocationStrata = 0.9320, showing good agreement between the actual and simulated LULC map. Analysis of the historical LULC changes depicted that during 2001–2021, the significant increase of agricultural land (14317 ha) and barren area (9063 ha), and the sharp decline of grassland (26215 ha), and forest cover (5989 ha) were the major LULC changes in the Chalus watershed. The model predicted that forest cover will continue to decrease from 29.46 % (50720.2667 ha) in 2021 to 25.67 % of area (44207.78694 ha) in 2040, as well as, unceasing expansion of barren area, agricultural land, and built-up area will be expected by 2040. Therefore, understanding the spatiotemporal dynamics of LULC change is extremely important to implement essential measures and minimize the destructive consequences of these changes.**

***Index Terms*—Change prediction, decision forest, deforestation, land use and land cover (LULC) change analysis, Markov chain model, segmentation classification.**

I. Introduction

LAND-USE/LAND-COVER (LULC) plays an important role in environmental processes, climate features, and biodiversity. Therefore, many studies have been carried out on monitoring and forecasting of LULC dynamics [1]–[3]. LULC changes, including deforestation, agricultural expansion because of population growth and more demand for crops, residential area development, and reduction of pasture areas, have destructive effects on the ecosystem. LULC changes, especially in the form of deforestation, cause an increase in greenhouse gas emissions and release large amounts of CO_2 into the atmosphere, which contribute to global warming and disrupt normal weather patterns [4]–[6]. In addition, deforestation and conversion of land from pasture to agricultural or residential uses increase the occurrence of floods, soil degradation, landslides, drought, air pollution, desertification, and biodiversity loss and also affect the quantity and quality of surface water and groundwater resources [7], [8]. Assessment of LULC change detection and prediction can provide important policy recommendations for advanced ecosystem management, studying global environmental change, and monitoring natural disasters [9].

Geospatial modeling of LULC changes and urban expansion can be used by land use planners to determine and monitor the future trend, rate, location, and magnitude of LULC changes [10]–[13]. In recent years, RS and GIS have become important geospatial tools for effective decision-making in sustainable land management, city and regional planning, and natural resource assessment. RS and GIS techniques are the most widely used approaches for producing LULC maps of an area in different years with acceptable accuracy to aid users in evaluating LULC spatiotemporal changes to implement essential measures and manage natural resources sustainably [14]–[18]. Therefore, it is essential to classify and map LULC patterns and dynamics using multitemporal satellite images to analyze the changes in LULC for different decades and forecast the future pattern of LULC types with different methods and techniques as the land change modeler or (CA)-Markov chain model [19]. The CA-Markov is a hybrid model which can predict the transitions

Manuscript received 5 April 2022; revised 10 June 2022; accepted 6 July 2022. Date of publication 8 July 2022; date of current version 20 July 2022. This work was supported by the National Key Research and Development Program of China under Grant 2021YFC3200301, in part by the Postdoctoral Research Foundation of China under Grant 2020M682477, and in part by the Fundamental Research Funds for the Central Universities under Grant 2042021kf0053. *(Corresponding author: Aqil Tariq; Shujing Qin.)*

Sepideh Jalayer and Alireza Sharifi are with the Faculty of Civil Engineering, Shahid Rajaee Teacher Training University, Tehran 16785-163, Iran (e-mail: sepideh.jal@gmail.com; a_sharifi@sru.ac.ir).

Dariush Abbasi-Moghadam is with the Department of Electrical Engineering, Shahid Bahonar University of Kerman, Kerman 76169-14111, Iran (e-mail: abbasimoghadam@uk.ac.ir).

Aqil Tariq is with the State Key Laboratory of Information Engineering in Surveying, Mapping and Remote Sensing, Wuhan University, Wuhan, China, and also with the Department of Wildlife, Fisheries and Aquaculture, Mississippi State University, Mississippi State, MS USA (e-mail: aqiltariq@whu.edu.cn).

Shujing Qin is with the State Key Laboratory of Water Resources and Hydropower Engineering Science, Wuhan University, Wuhan 430072, China (e-mail: shujing.qin@whu.edu.cn).

Digital Object Identifier 10.1109/JSTARS.2022.3189528

or spatiotemporal dynamics of LULC classes [20], [21]. The land change modeler (LCM) is based on transition probability matrices produced by the Markov chain and transition potential maps produced by training the support vector machine (SVM), MLP, logistic regression, decision forest, WNL, or SimWeight options.

Image classification is the most significant technique used in remote sensing for creating thematic maps from satellite imagery [22]. Several methods have been developed to classify LULC types. For instance, Talukdar *et al.* [3] utilized six machine learning algorithms for LULC mapping, namely fuzzy ARTMAP, RF, ANN, Mahalanobis distance, SAM, and SVM, to evaluate the accuracy of different algorithms and identify the best machine learning LULC classifier. Din and Mak [23] analyzed the LULC changes in Hyderabad during the years 1979–2020, and SVM algorithm was applied for the supervised classification of different acquired Landsat data. In their study, Liu and Li *et al.* used Landsat images and a RF classifier based on the GEE platform for LULC mapping in the Ganan prefecture. In this article, spectral indexes (NDVI, NDBI, and MNDWI) were calculated for each image and 11 potential factors were specified to evaluate their influences on LULC dynamics [24]. Wang *et al.* [25] classified Landsat 5 and 8 images for the years 1990 and 2010 using MLC in the ERDAS imagine and ArcGIS. Then LULC classified maps were imported to the CA-Markov model to detect and predict LULC changes.

Many researchers have been applying various geospatial modeling of LULC changes to evaluate the important impacts of future LULC patterns [26]. For instance, Leta *et al.* [27] analyzed the LULC spatiotemporal changes in the Nashe watershed using the MLC technique and predicted LULC maps for the years 2035 and 2050 by considering the potential driver variables. Abijith and Saravanan [28] applied random forest classification to produce the LULC maps on the Northern TN coast and employed the CA-Markov modeling approach to simulate LULC maps of 2025 and 2030. This research aims to detect LULC changes in the Chalus watershed during 2001–2021 using a hybrid approach between segment-based and pixel-based classification, which provides more accurate results for large study areas. In this research, the transition potential maps and the transition probability matrices for the years 2021 and 2040 are provided by the SVM algorithm and the Markov chain model, respectively, to project the 2021 and 2040 LULC maps of the Chalus watershed. Therefore, in this study SVM algorithm has been utilized to produce the transition potential maps of this densely study area which has the better results than other algorithms that have been used in previous studies such as MLP, logistic regression, WNL, or SimWeight.

II. Materials and Methods

A. Study Area

The Chalus watershed, with an area of 1721.932 km^2 , is located in the west part of Mazandaran Province. Mazandaran Province is the most populous province in Iran, which is located in the south of the Caspian Sea. The Chalus watershed extends between 36° 10′ 0″ N to 36° 40′ 0″ N latitudes and 51° 0′ 0″ E to 51° 40′ 0″ E longitudes and this region is very sensitive to both LULC change and climate change. The land cover includes built-up area, forest, garden, barren area, agricultural land, water body, grassland, and shrubland, and the annual rainfall ranges from 600 to 700 mm. The minimum and maximum heights of the Chalus watershed are −30 m and 4259 m, respectively, and the average slope of the basin is 41.63°. Fig. 1 depicts the location of the Chalus watershed in Iran.

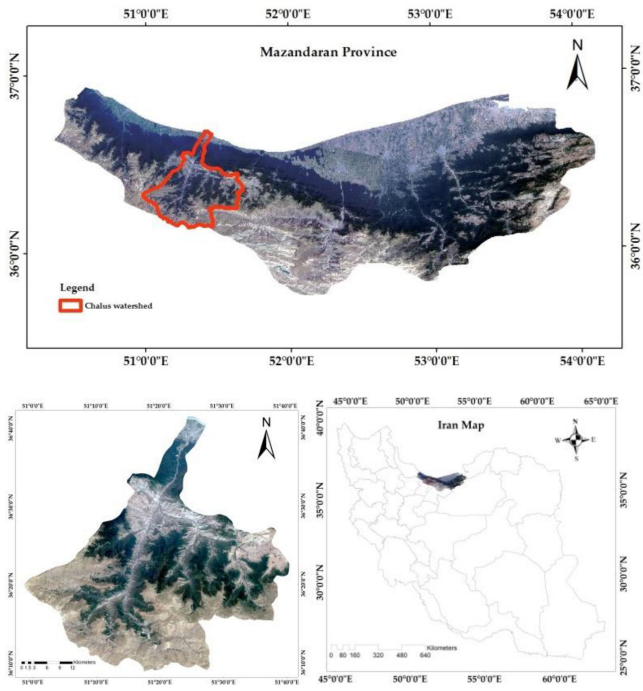

Fig. 1. Geographical location of the Chalus watershed in the province and country.

B. Datasets and Preprocessing

In this study, three Landsat images of the ETM + (for the year 2001) and OLI (for the years 2014 and 2021) sensors have been used for LULC classification and analysis in the Chalus watershed (Table I). Landsat data archive having images sufficiently consistent with data from the earlier missions allows assessing long-term (since 1972) regional and global LULC changes. The Landsat dataset were acquired in the same month for each year to avoid extreme differences in the LULC reflectance dataset [27]. Other geospatial data including digital elevation model (DEM), the study area boundaries, and geographic features such as stream networks, road networks, built-up areas, and forest cover of the Chalus watershed in the shapefile format (points, lines, and polygons) collected from the Iran National Cartographic Center, to produce topographic and distance driver variables for LULC simulation of the study area. These datasets were imported in ArcGIS 10.7.1, ENVI 5.3, ENVI Classic, and TerrSet software to produce LULC maps and predict the LULC trends for the study area. Then, the ground truth points of the Chalus watershed obtained from the high-resolution images of the Google Earth and field sampling were used for accuracy assessment. The flow

TABLE I
LANDSAT DATA CHARACTERIZATION FOR LULC CHANGE ANALYSIS IN THE CHALUS WATERSHED

Satellite sensor	Acquisition time	Path/Row	Spatial resolution	Bands used
Landsat7,ETM+,C1,Level1	2001/06/26 2001/06/03	165/35 164/35	30 m, 15 m	MS, PAN
Landsat8,OLI,C1,Level1	2014/06/06	165/35	30 m, 15 m	MS, PAN
Landsat8,OLI,C1,Level1	2021/06/25 2021/06/02	165/35 164/35	30 m, 15 m	MS, PAN

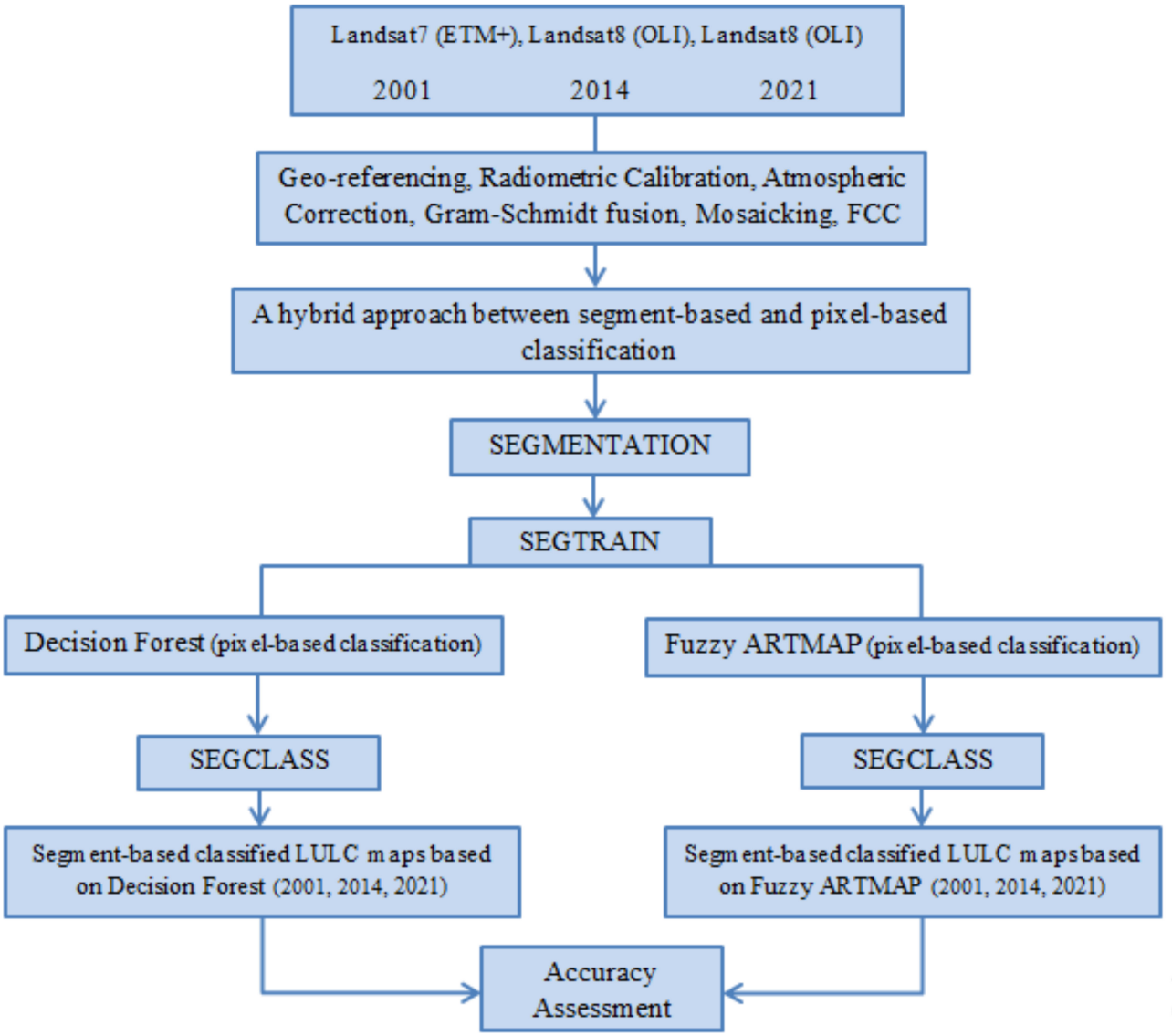

Fig. 2. Methodological framework for LULC classification.

chart for LULC classification to produce LULC maps of the Chalus watershed has been shown in Fig. 2.

The projection systems of all Landsat images and shapefiles were georeferenced to the WGS 84/UTM zone 39 N projection system [29], [30]. In ENVI 5.3 software, the radiometric calibration was performed in order to transform data's DN values to spectral radiance (at the sensor). Then, an atmospheric correction was done to all Landsat images by using FLAASH algorithm in ENVI 5.3 software [23], [29]. Following that, we used pixel-level image fusion to improve the spatial resolution of multispectral satellite images from the ETM+ and OLI sensors while retaining the multispectral image's spectral information in the fused image.

Thus, we used the Gram–Schmidt pan-sharpening approach to combine the spectral information of a low-resolution multispectral image (30 m) with the spatial information of a

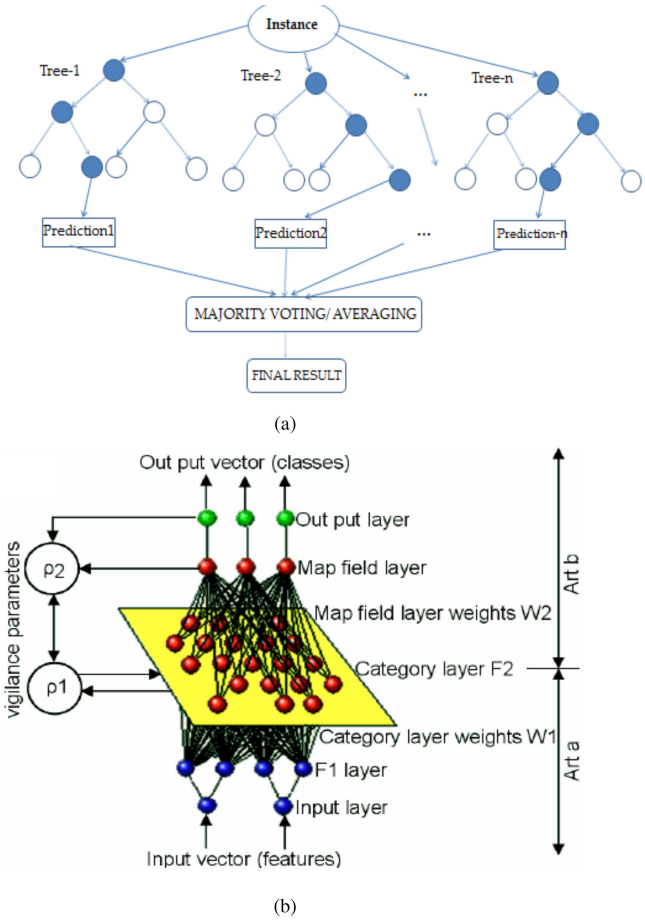

Fig. 3. Schematic architecture of LULC classifiers. (a) Decision forest. (b) Fuzzy ARTMAP.

high-resolution panchromatic image (15 m) to obtain a high-resolution MS image with a spatial resolution of 15 m [31]. Due to the problem of cloud cover in optical satellite imagery, which causes to miss information in images, mosaicking the cloud-free areas in the Landsat images for the years 2001 and 2021 was conducted to generate cloud-free composite scenes. Then, the spatial analyst extension was used to subset the cloud-free Landsat images and shapefiles to the region of interest in ArcGIS 10.7.1 software. Afterward, the false color composite of images (RGB = 43,2 for ETM+ and RGB = 54,3 for OLI) were created in TerrSet software before LULC classification.

C. LULC Classification

In this study, a hybrid approach between segment-based and pixel-based classification [32] was applied in TerrSet software to classify eight land use/cover categories including built-up area, forest, garden, barren area, agricultural land, water body, grassland, and shrubland in the Chalus watershed for the years 2001, 2014, and 2021. In this research, decision forest and fuzzy ARTMAP algorithms were implemented to produce pixel-based classified maps of Landsat images (Fig. 3). Decision forest is a supervised machine learning algorithm based on the concept of ensemble learning that can be used for both classification as well as regression. This algorithm consists of many decision trees and predicts the final output based on majority voting or averaging of the predictions from trees in the entire forest [33]. In addition, in the LULC classification of satellite images, it is difficult to demarcate between some pairs of land use/cover types; hence, a strategy of pattern classification based on fuzzy logic has been conducted for LULC classification. In recent years, an adaptive resonance theory (ART) map consists of two ART modules (ART_a, ART_b) based on neural networks incorporating fuzzy learning, namely fuzzy ARTMAP has been utilized for pattern classification [3], [34].

The hybrid approach between segment-based and pixel-based classification consists of three modules: Segmentation, SEGTRAIN, and SEGCLASS. In the first stage, the segmentation module was used to group pixels with a homogeneous spectral similarity into specific segments to create an image comprised of segments [32]. A moving window (3∗3) evaluated the variance and segments were demarcated relying on a specified similarity threshold. A larger similarity threshold will result in more generalized, less homogeneous segments, and the number of segments in the output image will be fewer [32]. In the second stage, the SEGTRAIN module was applied to create training sites and signature classes from the image segments. This module assigned the segments to specific land use/cover types to develop training sites and signatures. Once the training sites were defined, we started the classification stage. In our case, we imported the segment-based signatures we just created to run decision forest, and fuzzy ARTMAP classifiers to use the pixel-based classified images as our reference images for the SEGCLASS module. In the last stage, the SEGCLASS module was used to classify segments based on a pixel-based classified image obtained through decision forest, and fuzzy ARTMAP methods. The SEGCLASS module applied a majority rule algorithm to assign the majority class within each segment from the reference images. The SEGCLASS module can improve the accuracy of the pixel-based classified images and create smoother classified maps. Therefore, we employed a segmentation classification procedure by combining two pixel-based classifiers (decision forest and fuzzy ARTMAP) with segment-based classification for each Landsat image in 2001, 2014, and 2021 to create LULC maps of the Chalus watershed.

D. Accuracy Assessment of Classified Maps

The accuracy assessment of the segment-based classified maps using decision forest, and fuzzy ARTMAP is required before LULC change detection and future prediction. The validation of segmentation classification was implemented using the Confusion Matrix tool in ENVI Classic 5.3 through the ground truth points of the Chalus watershed obtained from Google Earth and field sampling. Therefore, kappa coefficient, overall accuracy, user's, and producer's accuracy of the classified LULC maps were computed for assessment [27], [35].

$$OA = \frac{\sum_{i=1}^{r} D_{ii}}{\mathrm{N}} \tag{1}$$

$$UA = \frac{\sum_{i=1}^{r} D_{ij}}{X_{+i}} \tag{2}$$

$$PA = \frac{\sum_{i=1}^{r} D_{ij}}{X_{i+}} \tag{3}$$

$$K = \frac{N\sum_{i=1}^{r} X_{ii} - \sum_{i=1}^{r}(X_{i+} * X_{+i})}{N^2 - \sum_{i=1}^{r}(X_{i+} * X_{+i})} \tag{4}$$

where N: total number of values, r: number of rows, D_{ii} : number of total correct values, D_{ij}: number of correct values in row i, D_{ij}: number of correct values in column j, X_{ii}: number of values in row i and column i, X_{+i} and X_{i+}: the column total and row total, respectively [18], [27].

E. Modeling and Predicting LULC Spatiotemporal Changes

TerrSet is an extensive set of procedures for image restoration, enhancement, transformation, and classification of remotely sensed imagery. In this study, the LCM in TerrSet software [36] was used to analyze LULC dynamics between two periods and predict the future pattern of LULC by using transition potential maps and transition probability matrices. Therefore, simulation and prediction of LULC changes in the Chalus watershed for the years 2021 and 2040 were carried out by following these four steps: first, LULC change assessment, second, LULC transition potential modeling, third, LULC change prediction, and fourth, validation of SVM-MC model output.

F. LULC Change Assessment

The LULC maps of 2001 with 2014, 2014 with 2021, and 2001 with 2021 were compared with analyze LULC changes in the Chalus watershed. The change analysis evaluates the quantitative changes, by charting gains and losses, between various LULC classes [36], [37]. Thus, the dominant transitions among different LULC types between two different years, and net changes for each LULC class were calculated [35], [36].

G. LULC Transition Potential Modeling

LULC transitions in the Chalus watershed that existed between the two LULC maps were grouped into submodels. Then, several driving factors such as DEM, slope, distance from road, distance from stream, distance from built-up area, distance from forest, and evidence likelihood rasters were selected as the potential driver factors that influence LULC changes and were tested based on Cramer's V coefficient [27], [35], [38]. Geographic features such as stream networks, road networks, built-up areas, and forest cover of the Chalus watershed in the shapefile format were imported into ArcGIS 10.7.1 to extract distance driver variables using Euclidean distance procedure. The evidence likelihood rasters were prepared based on a Boolean map of areas that have gone through the transition between two different years and a categorical variable that has been binned into classes. The importance of each variable was determined using Cramer's V, that a high Cramer's V demonstrates the potential explanatory value of the variable is acceptable [39]. Afterward, the modeling of transition submodels was implemented by using SVM algorithm in TerrSet software to generate transition potential maps. They are the pixels that underwent the transitions from one LULC type to another being modeled also the pixels that had the potential to change in certain periods [40].

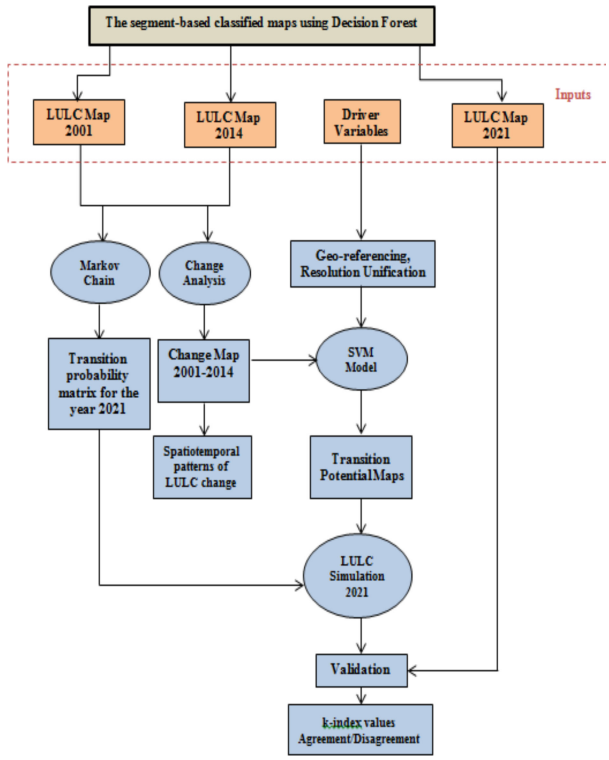

Fig. 4. Flowchart for LULC simulation.

H. LULC Change Prediction

The Markov chain model determines the chance of transitioning from one LULC type to another and creates a transition probability matrix utilizing the earlier and later LULC maps, as well as the date supplied as the prediction date, based on a future projection of the transition potentials [27], [40]. LCM provides two kinds of change prediction, namely soft and hard prediction [36]. Hard prediction is based on multiobjective land allocation module [36], [40], [41], and soft prediction provides a continuous mapping of vulnerability to change, in which each pixel is dedicated a value between 0 and 1 [27], [41]. In this study, the hard prediction was used to create LULC maps of the Chalus watershed with the same categories as the inputs for the years 2021 and 2040. The simulated LULC map of 2021 was produced by using 2001 and 2014 classified maps, and the LULC maps of 2001 and 2021 were utilized to predict the LULC map of the Chalus watershed for the year 2040.

I. Validation of SVM-MC Model Output

The classified LULC maps of the 2001 and 2014 years were utilized to produce the simulated LULC map for 2021. Then, the simulated and the actual LULC map of 2021 were compared with calibrate and validate the LCM model. Kstandard, Klocation, Kno, and KlocationStrata [27] were calculated to evaluate the overall accuracy both in terms of location and quantity. The flowchart for LULC change detection during 2001–2014 and simulation the future pattern of LULC in the Chalus watershed for the year 2021 has been illustrated in Fig. 4.

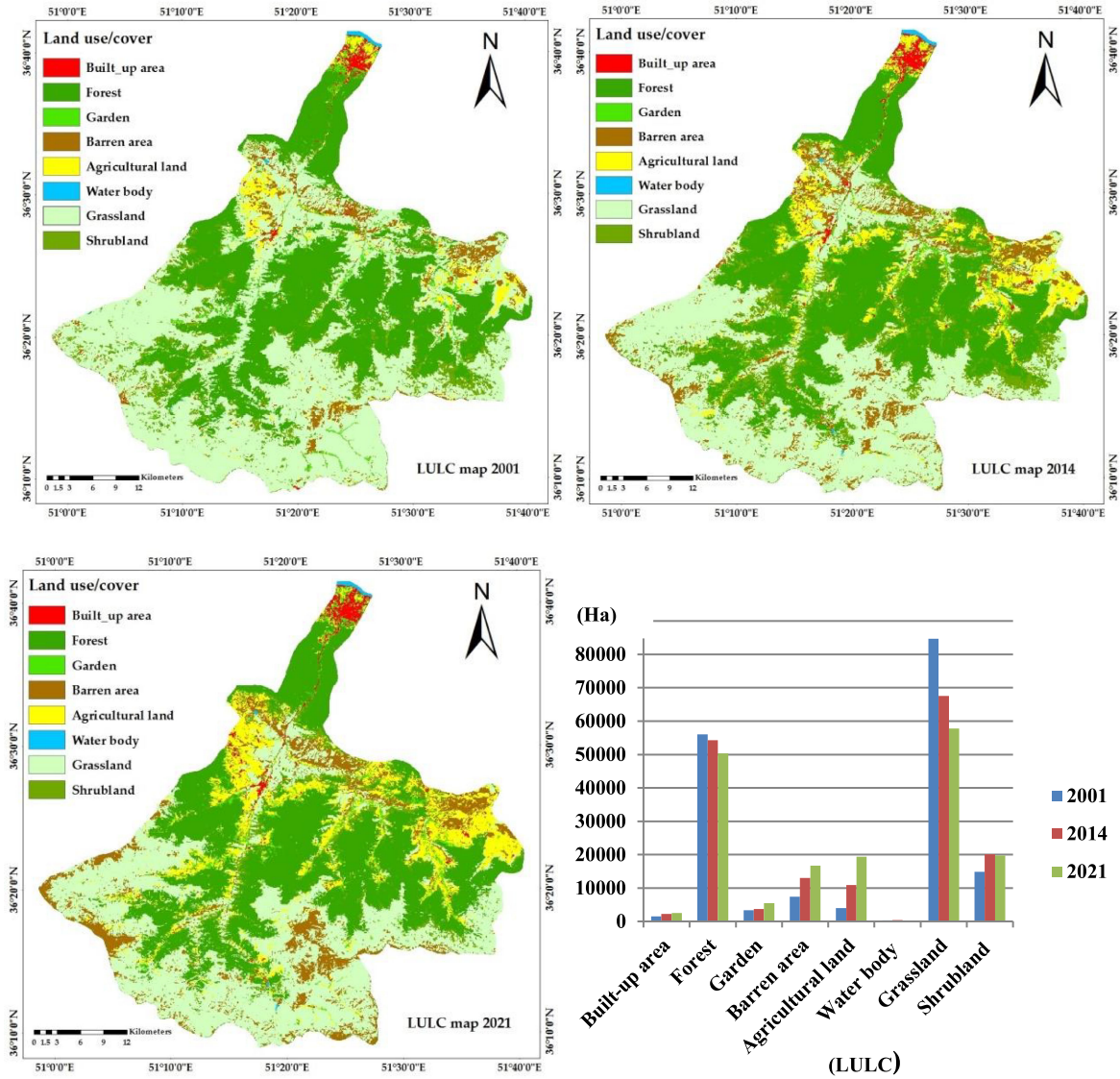

Fig. 5. LULC classified maps based on decision forest for the years 2001, 2014, and 2021, and the area of LULC classes (ha).

III. Results and Discussion

A. Accuracy Assessment of LULC Classification

The LULC classified maps of the Chalus watershed for the years 2001, 2014, and 2021, and the area of LULC classes (ha) are shown in Figs. 5 and 6. The accuracy assessment of LULC maps can provide the degree of confidence in the results to evaluate different classification methods. For accuracy assessment, the segment-based classified maps using decision forest and fuzzy ARTMAP pixel-based classification were compared with the ground truth points of the Chalus watershed obtained from the high-resolution images of the Google Earth and field sampling. Therefore, kappa coefficient, overall accuracy, user's and producer's accuracy of the LULC maps were produced by generating confusion/error matrix (Tables II and III). The results show that combining decision forest pixel-based classifier with segment-based classification has the highest accuracy in LULC classification, as shown in Table II, the overall accuracy was 95.4286 %, 96.1631 %, and 97.1429 % for the years 2001, 2014, and 2021, respectively. Therefore, in the next stages of the research, the segment-based classified maps using decision forest have been used to analyze LULC changes for different periods and forecast the future pattern of LULC in the Chalus watershed.

B. Analyzing LULC Changes

The area coverage of different LULC categories in the Chalus watershed for the years 2001, 2014, and 2021 were calculated (Table IV). Grassland is the main LULC class in the Chalus watershed which covered 48.85 % of the area in 2001, 38.48 % in 2014, and 33.64 % in 2021. Forest covered an area of 32.93 % (56709.21 ha) in 2001 but decreased substantially to 31.70 % (54598.95 ha) in 2014 and 29.46 % (50720.26 ha) in 2021, respectively. Agricultural land increased from 2.75 %

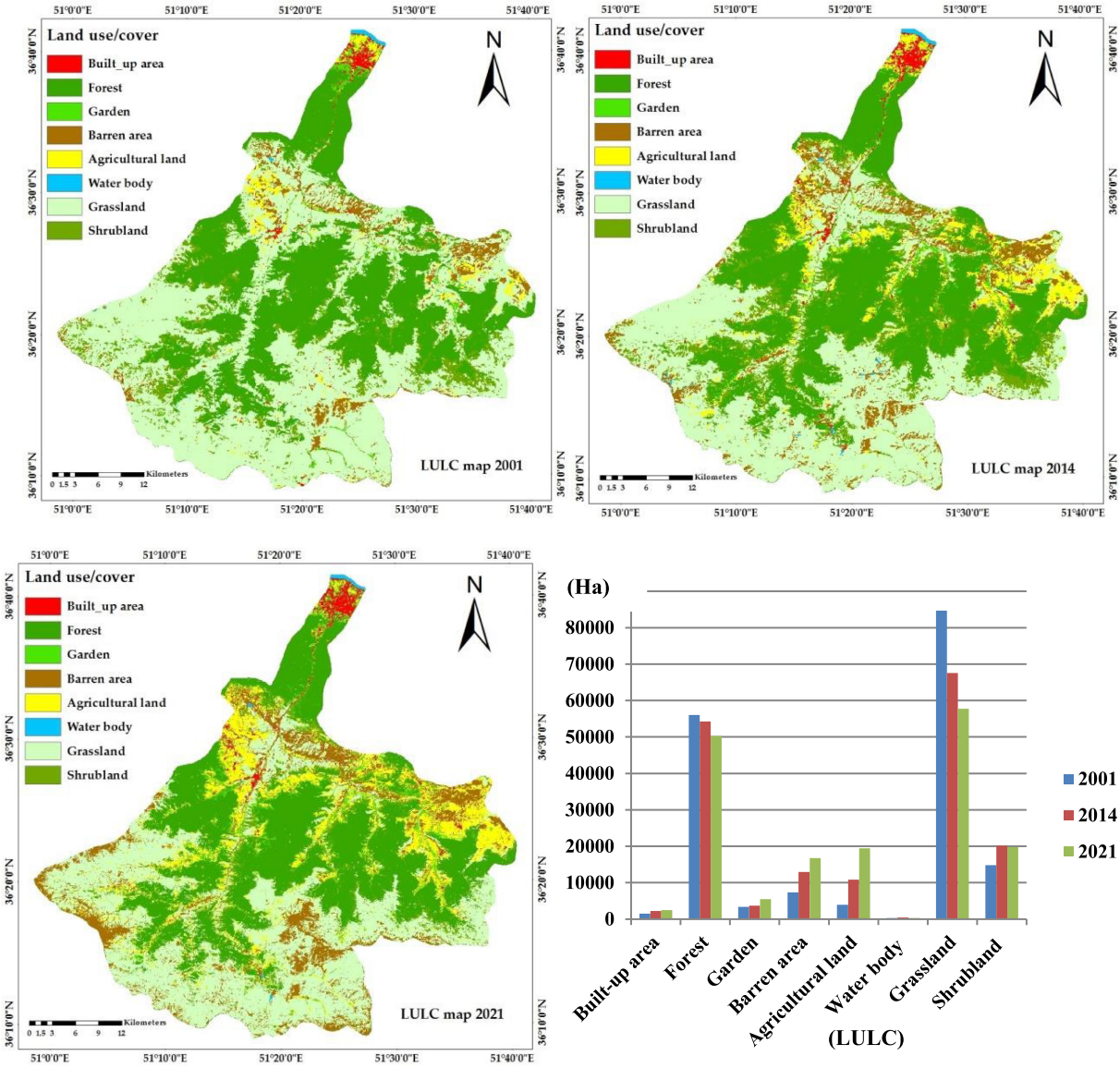

Fig. 6. LULC classified maps based on fuzzy ARTMAP for the years 2001, 2014, and 2021, and the area of LULC classes (ha).

TABLE II
ACCURACY OF THE SEGMENT-BASED CLASSIFIED MAPS USING DECISION FOREST FOR THE YEARS 2001, 2014, AND 2021

	2001		2014		2021	
LULC	**Prod.ACC**	**User ACC**	**Prod.ACC**	**User ACC**	**Prod.ACC**	**User ACC**
Built-up area	96.00	100	98.40	95.85	98.67	96.10
Forest	100	95.00	100	100	100	97.44
Garden	91.67	91.67	89.36	91.30	91.67	94.29
Barren area	100	86.36	96.67	100	100	92.68
Agricultural land	93.75	97.83	89.06	98.28	95.83	100
Water body	100	88.24	100	100	100	100
Grassland	100	96.30	100	91.18	100	100
Shrubland	84.62	100	100	100	92.31	96.00
Overall accuracy	95.4286 %		96.1631 %		97.1429 %	
Kappa coefficient	0.9452		0.9478		0.9657	

TABLE III
ACCURACY OF THE SEGMENT-BASED CLASSIFIED MAPS USING DECISION FOREST FOR THE YEARS 2001, 2014, AND 2021

	2001		2014		2021	
LULC	**Prod.ACC**	**User ACC**	**Prod.ACC**	**User ACC**	**Prod.ACC**	**User ACC**
Built-up area	98.63	96.00	97.26	98.61	98.40	96.35
Forest	97.73	93.48	100	97.78	100	100
Garden	63.41	96.30	90.24	100	89.36	91.30
Barren area	93.10	84.38	93.10	81.82	96.67	100
Agricultural land	83.87	88.14	88.71	100	89.06	96.61
Water body	100	100	100	100	100	100
Grassland	100	75.56	100	79.07	96.77	88.24
Shrubland	89.74	92.11	87.18	91.89	100	100
Overall accuracy	90.4070 %		94.1860 %		95.9233 %	
Kappa coefficient	0.8883		0.9324		0.9446	

TABLE IV
AREA COVERAGE OF LULC CLASSES IN THE CHALUS WATERSHED FOR THE YEARS 2001, 2014, AND 2021

	Area					
	2001		2014		2021	
LULC	**Ha**	**% of area**	**Ha**	**% of area**	**Ha**	**% of area**
Built-up area	1486.509	0.863	2277.3742	1.322	2401.9659	1.394
Forest	56709.2141	32.933	54598.9591	31.707	50720.2667	29.46
Garden	3922.3669	2.278	3787.9473	2.2	5151.3268	2.9915
Barren area	7292.7746	4.237	12750.2732	7.405	16355.6959	9.498
Agricultural land	4748.5403	2.758	11747.0402	6.823	19065.3179	11.072
Water body	307.2062	0.178	303.3605	0.176	265.3983	0.154
Grassland	84130.3842	48.858	66264.2725	38.482	57915.527	33.64
Shrubland	13596.2148	7.895	20463.9834	11.885	20317.7118	11.79
Total	**172193.2**	**100**	**172193.2**	**100**	**172193.2**	**100**

(4748.54 ha) in 2001 to 6.823 % (11747.04 ha) in 2014 and 11.07 % (19065.31 ha) in 2021, respectively. Similarly, Barren area increased from 4.237 % of the study area (7292.7746 ha) in 2001 to 9.498 % (16355.6959 ha) in 2021. Built-up area covered an area of 0.863 % (1486.509 ha) in 2001, and increased substantially to 1.322 % (2277.3742 ha) in 2014 and 1.394 % (2401.9659 ha) in 2021, respectively (Table IV). In addition, the spatiotemporal changes between different LULC categories in the Chalus watershed during the period 2001, 2014, and 2021 were analyzed (Table V). During 2001–2021, the net change area of built-up area, forest, garden, barren area, agricultural land, water body, grassland, and shrubland were 915, −5989, 1229, 9063, 14317, −42, −26215, and 6721 hectares (Table V). Grassland to agricultural land (12548 ha), grassland to barren area (9157 ha), and forest to shrubland (5611 ha) changes had the highest LULC transition area for 2001–2021 (Fig. 7). During 2001–2021 period, the spatial coverage of grassland continued to decrease. Moreover, the development of built-up area is differed from 53.2 % (790.86 ha) during 2001–2014 to 5.47 % (124.59 ha) during 2014–2021. This increase (61.55 %) in built-up area during 2001–2021 leads to a decrease in grassland (511 ha), agricultural land (201 ha), garden (197 ha), shrubland (71 ha), forest (20 ha), and water body (16 ha) (Fig. 8).

Thus, 12548 ha, 9157 ha, 2445 ha, 1382 ha, 511 ha, and 180 ha of grassland have been converted into agricultural land, barren area, shrubland, garden, built-up area, and forest, respectively, between 2001 and 2021. During the same time period, the proportion of water body has decreased from 307.20 ha to 265.39 ha, with 16 ha, 8.5 ha, 16 ha, and 1.5 ha areas have been converted into built-up area, grassland, barren area, and shrubland, respectively.

Furthermore, the area being determined as garden decreased from 3922.3669 ha to 3787.9473 ha during the 2001–2014 period, and increased to 5151.3268 ha in 2021. Between 2001 and 2021, the majority of garden areas were being converted into agricultural land and (511 ha) and built-up area (197 ha), while part of grassland (1382 ha), forest cover (361 ha), and Shrubland (222 ha) have been converted into garden during these years. The gains and losses of different LULC categories in the Chalus watershed between 2001 and 2021 were calculated, as shown in Fig. 8. The significant increase of agricultural land, built-up area, barren area, shrubland, and the sharp decline of grassland,

TABLE V
NET CHANGES OF EACH LULC CATEGORY FOR 2001–2014, 2014–2021, AND 2001–2021

	Change								
	2001–2014			2014–2021			2001–2021		
LULC	Ha	%	% of area	Ha	%	% of area	Ha	%	% of area
Built-up area	790.86	53.2	0.459	124.59	5.47	0.072	915	61.55	0.53
Forest	−2110.255	−3.72	−1.226	−3878.7	−7.10	−2.247	−5989	−10.56	−3.47
Garden	−134.41	−3.42	−0.078	1363.3	35.99	0.7915	1229	31.33	0.714
Barren area	5457.49	74.83	3.168	3605.4	28.27	2.093	9063	124.27	5.26
Agricultural land	6998.49	147.38	4.065	7318.2	62.29	4.249	14317	301.5	8.31
Water body	−3.84	−1.24	−0.002	−37.96	−12.51	−0.022	−42	−13.67	−0.02
Grassland	−17866.11	−21.23	−10.376	−8348.74	−12.59	−4.842	−26215	−31.15	−15.22
Shrubland	6867.76	50.51	3.99	−146.27	−0.71	−0.095	6721	49.4	3.9

and forest cover were the major LULC changes in the Chalus watershed. During 2001–2021, gain and loss in forest cover was 3038 ha (5.1 %) and 9027 ha (−15.66 %), with a net loss of 5989 ha (−10.56 %). Grassland lost 30208 ha (−35.91 %) and gained 3993 ha (4.76 %), with a net loss of 26215 ha (−31.15 %). Built-up area increased with a net gain of 915 ha. Gain and loss in agricultural land was 15888 ha and 1571 ha, with a net gain of 14317 ha. The significant increase of barren area (9063 ha) between 2001 and 2021, has resulted in a decline in both grassland and agricultural land. The results show that rapid population growth has led to residential area development and agricultural expansion in the Chalus watershed. As well as, deforestation and reduction of pasture areas such as grassland in the study area due to human activities have affected all the functions of the watershed. For instance, deforestation and conversion of grassland to agricultural land in the Chalus watershed have led to barren area expansion, soil degradation, landslides, floods, and biodiversity loss. These LULC changes in the Chalus watershed have negatively affected the quantity and quality of surface water and groundwater resources of the basin. Therefore, the analysis of LULC changes is required to implement essential measures and minimize the destructive consequences of these changes.

C. LULC Transition Potential Modeling

Based on the observed LULC changes in the Chalus watershed for both study periods (2001–2014 and 2001–2021), the transition from forest to shrubland, forest to built-up area, agricultural land to barren area, garden to built-up area, garden to agricultural land, garden to grassland, barren area to built-up area, barren area to agricultural land, grassland to garden, agricultural land to built-up area, agricultural land to garden, grassland to built-up area, shrubland to garden, grassland to barren area, shrubland to forest, grassland to agricultural land, and shrubland to grassland were used to produce transition potential maps and predict LULC maps of the Chalus watershed for the years 2021 and 2040. The driver variables as static and dynamic components, including DEM, slope, distance from roads, distance from streams, distance from built-up areas, distance from forest, and evidence likelihood rasters (Fig. 9), were added to the model for both study periods, and the potential power of each driving factor by Cramer's V was examined (Table VI).

Then, the driver variables that had a Cramer's V value of about 0.15 or higher were used for LULC change modeling. In this research, variables as slope and distance from stream with low Cramer's V values 0.0134 and 0.1062 for 2001–2014, and 0.0155 and 0.1096 for 2001–2021, respectively, were not utilized as useful variables of transitions. Afterward, the modeling of transition submodels was applied by using the SVM algorithm to produce transition potential maps for both periods 2001–2014 and 2001–2021. Figs. 10 and 11 indicate the transition potential maps that show how much each LULC type has the potential to change to another LULC in certain periods.

A. Simulation and Prediction

The transition probability matrix for 2021, which predicts the likelihood that each LULC type would convert to another LULC type in 2021, was produced using the Markov chain model with 2001 and 2014 LULC classified maps. Then, LCM in TerrSet software was utilized to simulate the future pattern of LULC in the study area for the year 2021 by using the transition potential maps according to the changes between different LULC categories during the period 2001–2014, and transition probability matrix for the year 2021. The real and simulated LULC maps of the Chalus watershed for 2021 are shown in Fig. 12.

Table VII represents that forest and water body are the most stable LULC categories with respective probabilities of 0.9342 and 0.9048. Garden, shrubland, and agricultural land are the most dynamic LULC categories with transition probabilities of 0.5308, 0.6399, and 0.6636. In these LULC categories, grassland was mainly converted into agricultural land and barren area, whereas forest cover was primarily transformed into shrubland. Afterward, the transition probability matrix for 2040 was produced by the Markov chain model using 2001 and 2021 LULC layers (Table VIII). Then, LCM in TerrSet software was utilized to forecast the future pattern of LULC in the Chalus watershed for the year 2040 by using the transition potential maps

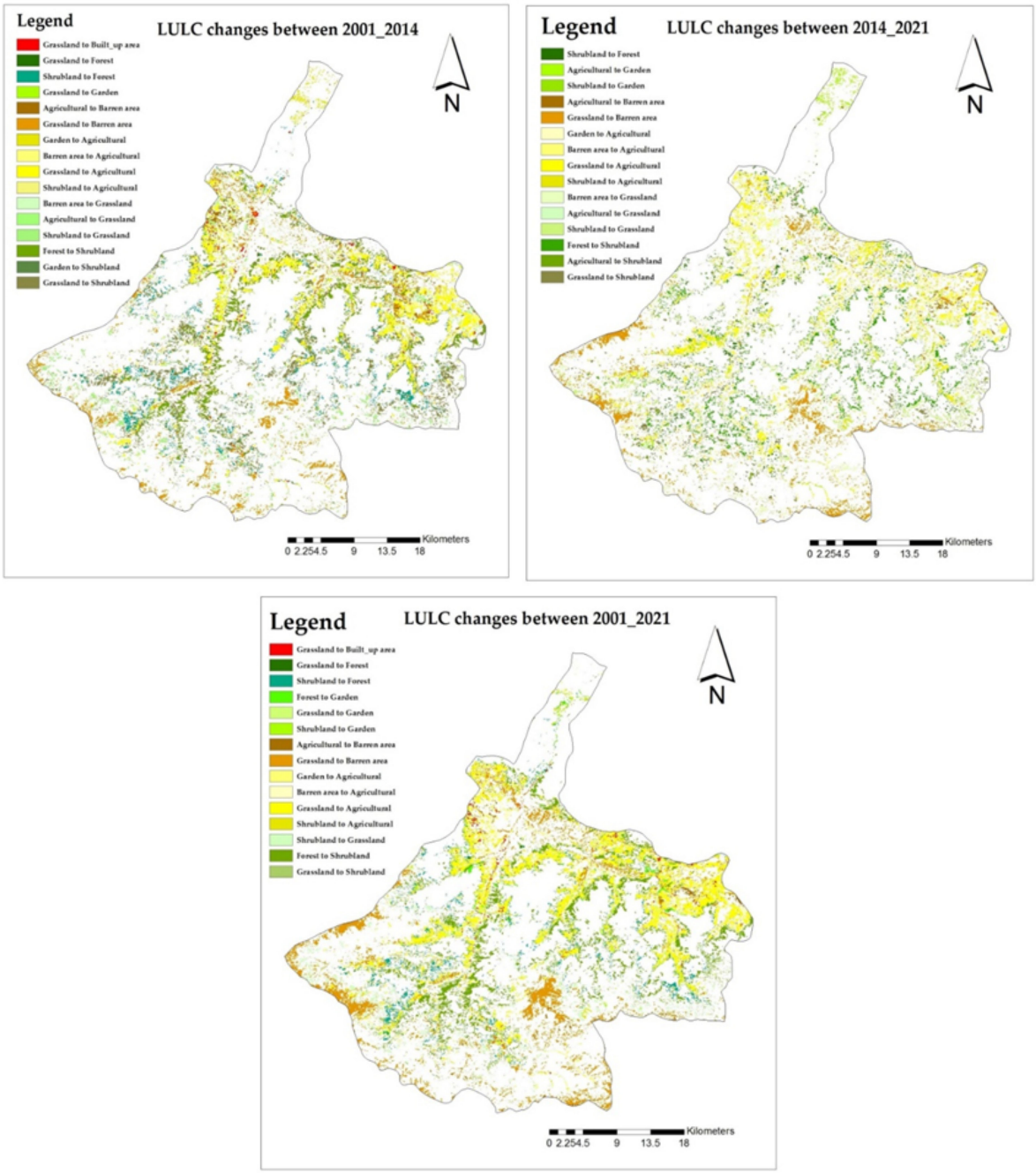

Fig. 7. Distribution of the LULC categories that transitioned between 2001–2014, 2014–2021, and 2001–2021.

TABLE VI
CRAMER'S V FOR EACH OF THE DRIVER VARIABLES

Driver variables		Evidence likelihood	Distance from built-up areas	Distance from forest	Distance from stream	Distance from roads	DEM	Slope
Cramer's V	**2001–2014**	0.4934	0.1831	0.3220	0.1062	0.1937	0.2302	0.0134
	2001–2021	0.4940	0.2062	0.3240	0.1096	0.2091	0.2573	0.0155

according to the changes between different LULC categories during the period 2001–2021 and transition probability matrix for the year 2040. Fig. 13 depicts the predicted LULC map for 2040, and the area of LULC classes (ha) for the years 2021 and 2040.

Table VIII represents that forest and barren area are the most stable LULC categories with respective probabilities of 0.8923 and 0.8519. Garden, shrubland, and grassland are the most dynamic LULC categories with transition probabilities of 0.6079, 0.6213, and 0.7456. In these LULC categories, grassland

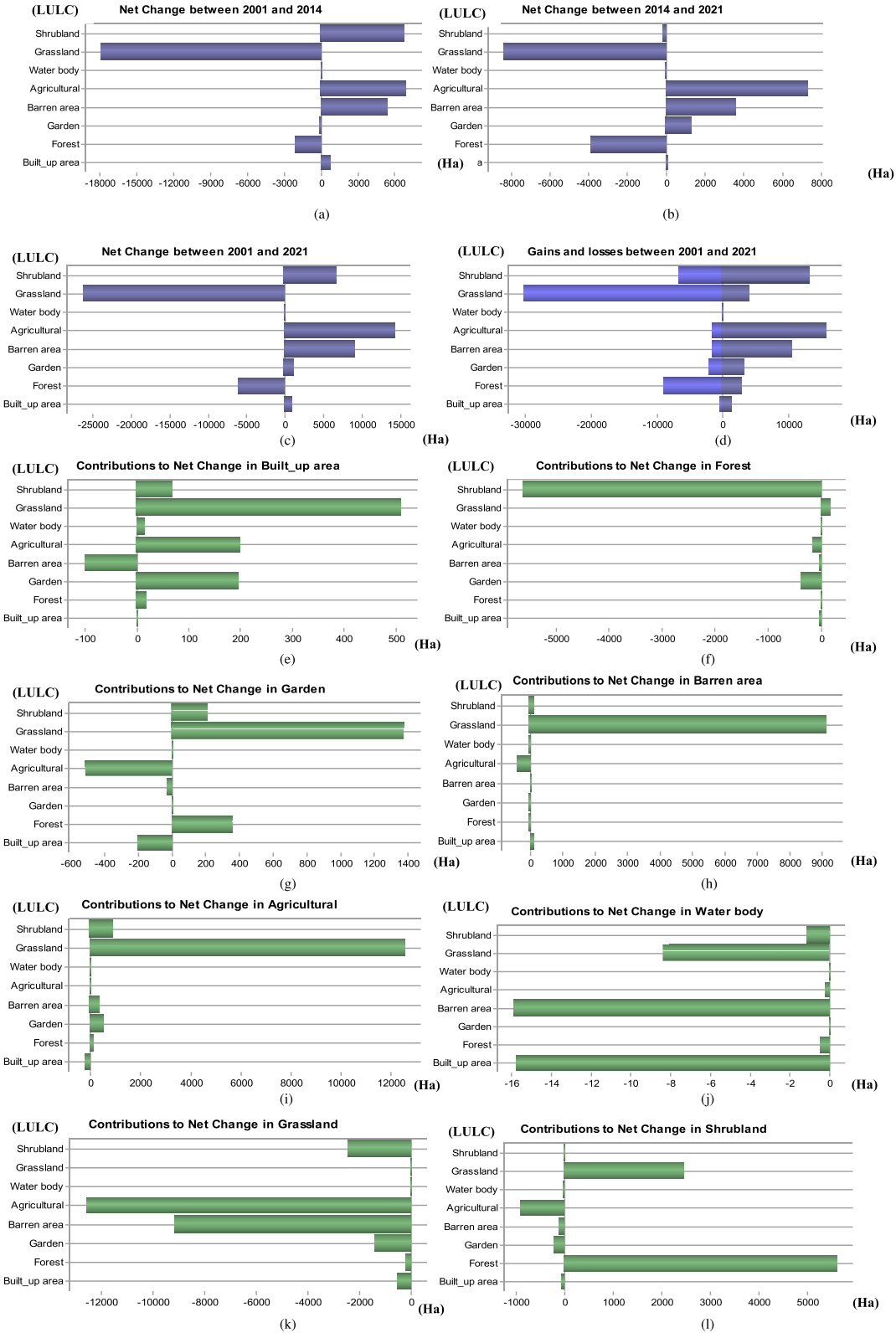

Fig. 8. Net change graph between (a) 2001–2014, (b) 2014–2021, and (c) 2001–2021. (d) Gains and losses graph between 2001 and 2021. (e) Contributions to net change (ha) in built-up area. (f) Forest. (g) Garden. (h) Barren area. (i) Agricultural land. (j) Water body. (k) Grassland. (l) Shrubland between 2001 and 2021.

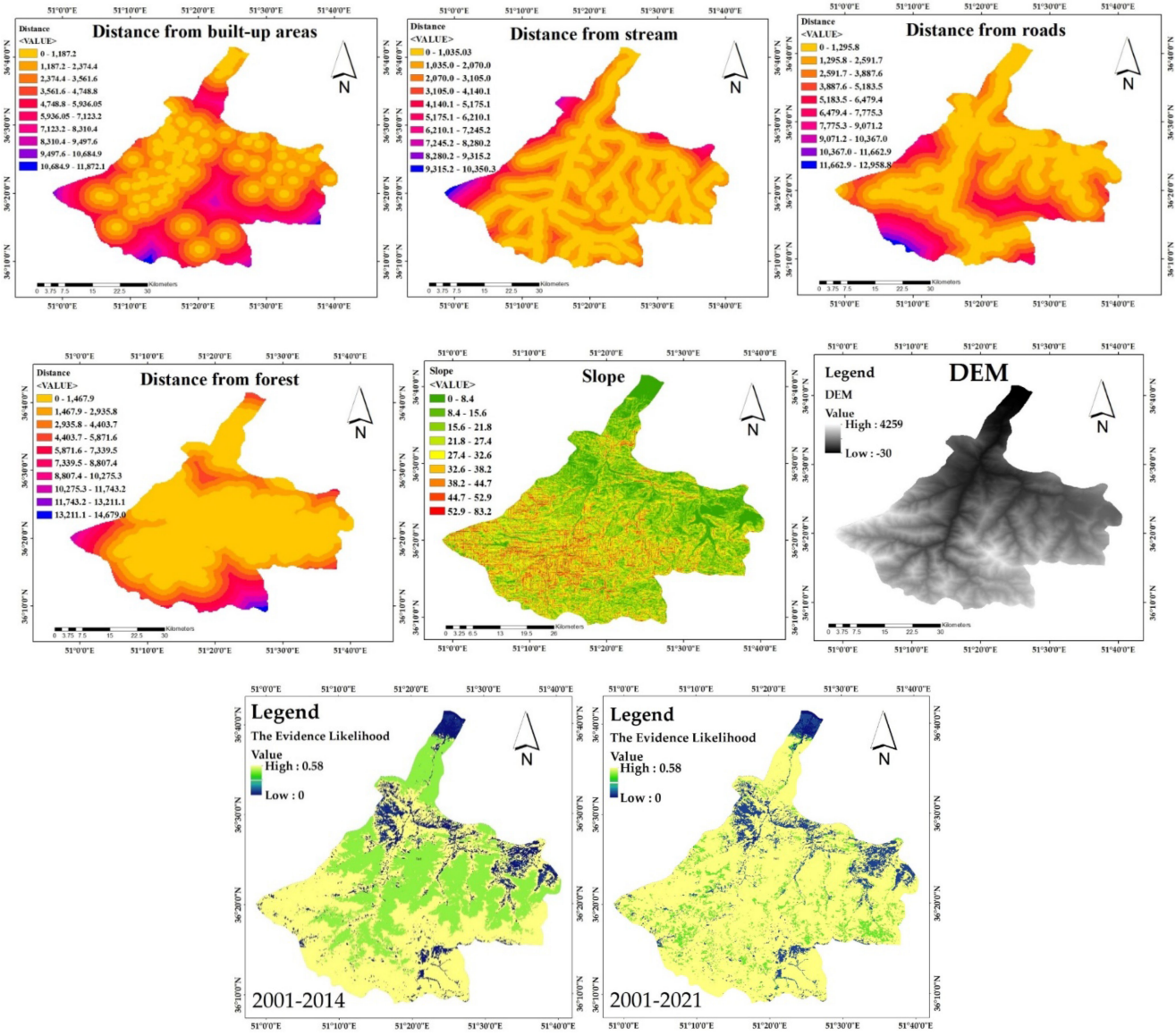

Fig. 9. Maps of the variables.

TABLE VII
TRANSITION PROBABILITY MATRIX OF LULC CLASSES FOR THE YEAR 2021

Classes	Built-up area	Forest	Garden	Barren area	Agricultural land	Water body	Grassland	Shrubland
Built-up area	0.8224	0.0045	0.0517	0.0460	0.0471	0.0025	0.0258	0.0000
Forest	0.0001	0.9342	0.0034	0.0005	0.0000	0.0000	0.0000	0.0618
Garden	0.0648	0.0225	0.5308	0.0000	0.1553	0.0003	0.0520	0.1742
Barren area	0.0568	0.0005	0.0000	0.8717	0.0680	0.0000	0.0030	0.0000
Agricultural land	0.0255	0.0002	0.0421	0.1378	0.6636	0.0002	0.1306	0.0000
Water body	0.0061	0.0026	0.0000	0.0015	0.0000	0.9048	0.0849	0.0001
Grassland	0.0026	0.0000	0.0070	0.0575	0.0708	0.0002	0.8233	0.0385
Shrubland	0.0016	0.1568	0.0319	0.0000	0.0366	0.0000	0.1331	0.6399

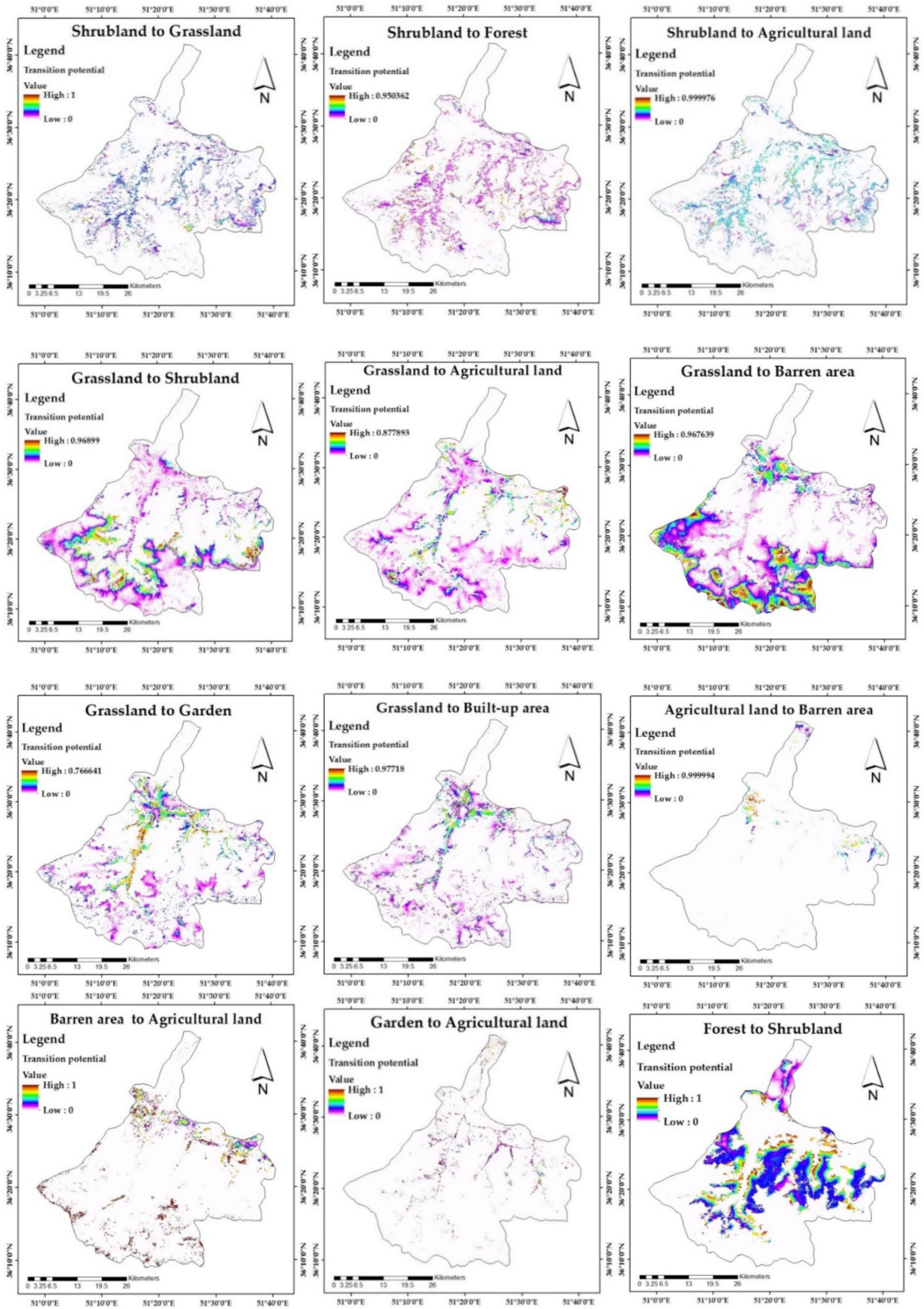

Fig. 10. Transition potential maps according to the changes between different LULC categories in the Chalus watershed during the period 2001–2014.

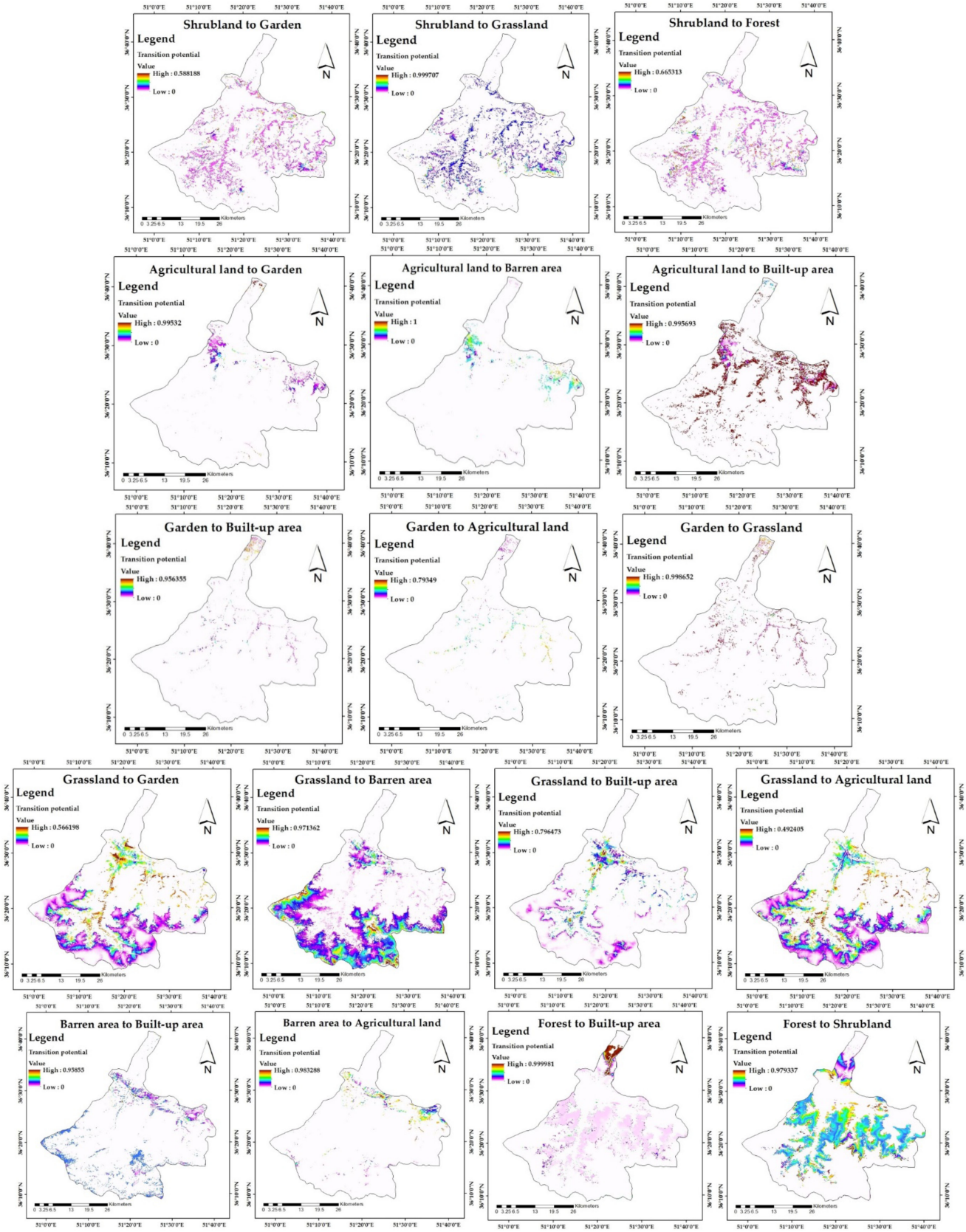

Fig. 11. Transition potential maps according to the changes between different LULC categories in the Chalus watershed during the period 2001–2021.

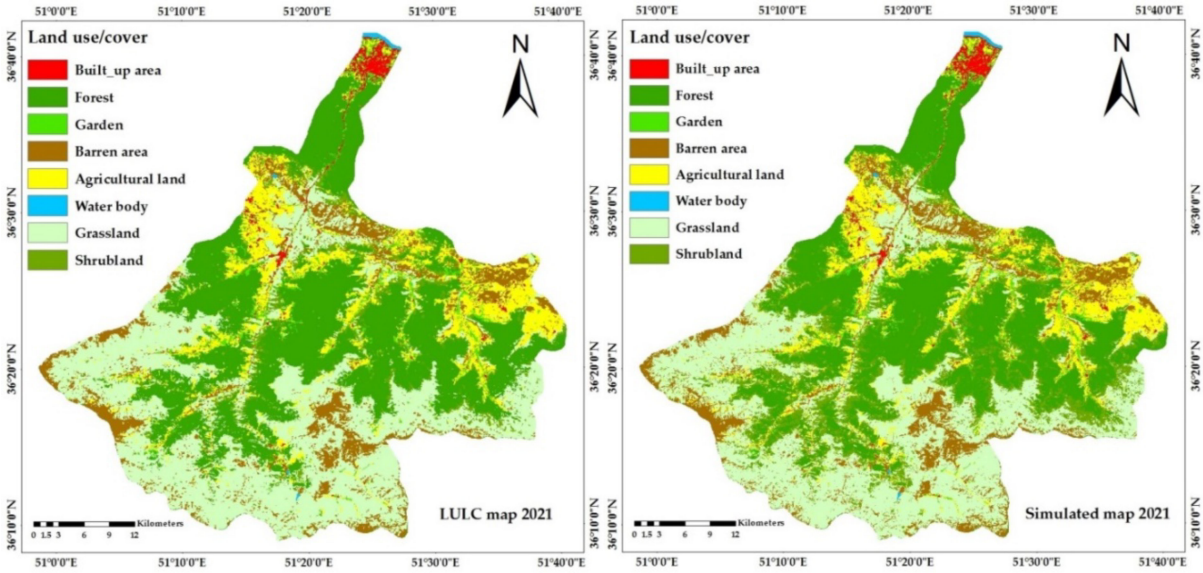

Fig. 12. Actual and simulated LULC maps.

TABLE VIII
TRANSITION PROBABILITY MATRIX OF LULC CLASSES FOR THE YEAR 2040

Classes	Built-up area	Forest	Garden	Barren area	Agricultural land	Water body	Grassland	Shrubland
Built-up area	0.8029	0.0028	0.0802	0.0752	0.0215	0.0010	0.0164	0.0000
Forest	0.0001	0.8923	0.0051	0.0009	0.0000	0.0000	0.0000	0.1017
Garden	0.0672	0.0336	0.6079	0.0000	0.1714	0.0001	0.0324	0.0874
Barren area	0.0031	0.0002	0.0000	0.8519	0.1093	0.0000	0.0349	0.0006
Agricultural land	0.0407	0.0000	0.0534	0.1073	0.7609	0.0000	0.0378	0.0000
Water body	0.0399	0.0048	0.0000	0.0288	0.0000	0.8302	0.0933	0.0030
Grassland	0.0012	0.0005	0.0111	0.0769	0.1121	0.0003	0.7456	0.0523
Shrubland	0.0015	0.1291	0.0380	0.0000	0.0409	0.0001	0.1691	0.6213

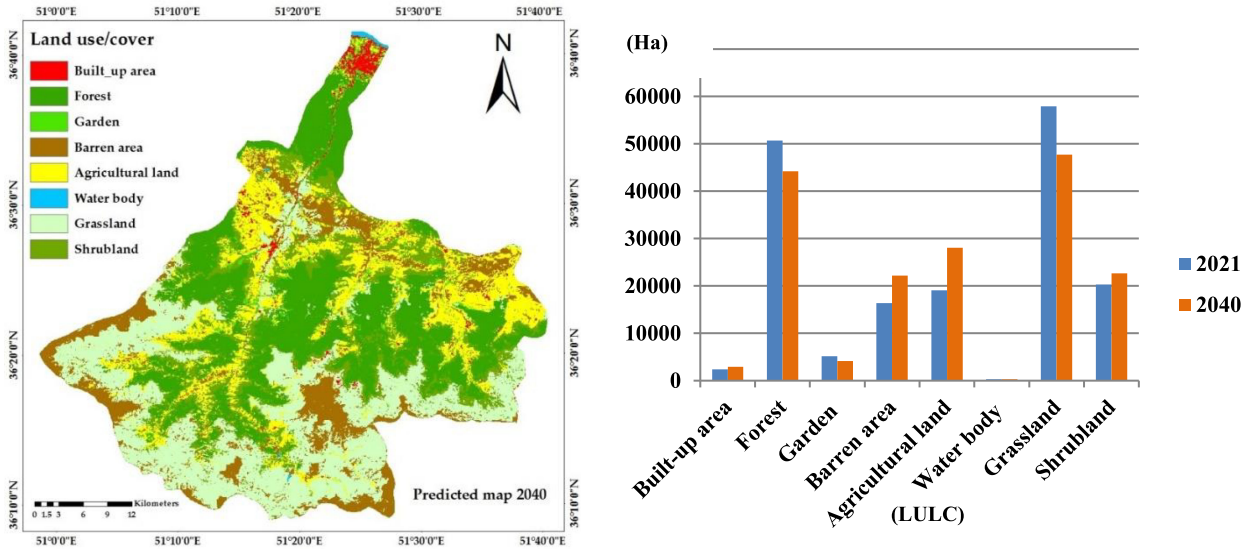

Fig. 13. Predicted LULC map for 2040 in the Chalus watershed, and the area of LULC classes (ha) for the years 2021 and 2040.

TABLE IX
AREA COVERAGE OF LULC CLASSES IN THE CHALUS WATERSHED FOR THE YEAR 2040, AND NET CHANGES OF EACH LULC CATEGORY BETWEEN 2021 AND 2040

	Area		Change		
	2040		2021–2040		
LULC	Ha	% of area	Ha	%	% of area
Built-up area	2962.596476	1.72	560.63	23.34	0.32
Forest	44207.78694	25.67	−6512.47	−12.83	−3.78
Garden	4133.430665	2.40	−1017.89	−19.75	−0.59
Barren area	22157.03297	12.86	5801.33	35.46	3.36
Agricultural land	28069.7666	16.30	9004.44	47.22	5.22
Water body	261.1883	0.151	−4.21	−1.58	−0.002
Grassland	47717.36715	27.72	−10198.15	−17.6	−5.92
Shrubland	22684.04158	13.17	2366.32	11.64	1.37
Total	**172193.2**	**100**			

TABLE X
AREA COVERAGE OF LULC CLASSES IN THE ACTUAL AND SIMULATED LULC MAPS OF THE CHALUS WATERSHED FOR 2021

	Actual	Simulated
LULC	Ha	Ha
Built-up area	2401.9659	2491.8730
Forest	50720.2667	50210.3222
Garden	5151.3268	5130.2171
Barren area	16355.6959	16930.5443
Agricultural land	19065.3179	19838.6554
Water body	265.3983	260.2131
Grassland	57915.527	57132.4334
Shrubland	20317.7118	20198.9523
Total	**172193.2**	**172193.2**

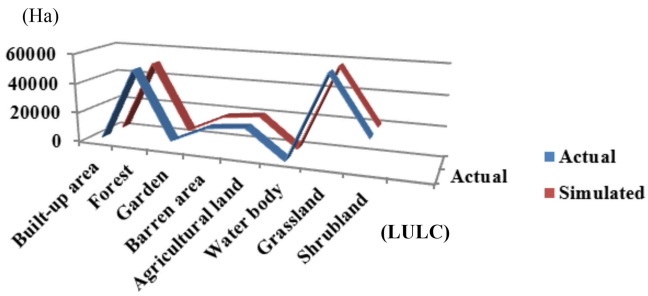

Fig. 14. Area of LULC classes (ha) graph in the actual and simulated maps.

was primarily transformed into agricultural land and barren area with respective transition probabilities 0.1121 and 0.0769, whereas forest cover was mainly converted into shrubland with a transition probability of 0.1017.

During 2001–2021, agricultural land increased to 11.072 % of area from 2.758 %, and predicted results represent that it will continue to increase to 16.30 % of area in 2040. As well as, Table IX shows that unceasing expansion of barren area will be expected from 9.498 % of area (16355.69 ha) in 2021 to 12.86 % of area (22157.032 ha) in 2040. In addition, built-up area and shrubland will show a positive growth till 2040 (0.32 % and 1.37 % of area). The model predicted that forest cover will continue to decrease to 44207.78 ha (25.67 % of area) in 2040. Between 2001 and 2021, the spatial coverage of grassland decreased to 57915.52 ha from 84130.3842 ha in 2001, and the predicted results show that it will continue to decrease to 47717.36 ha in 2040. These unintended modifications to LULC have a detrimental effect on ecosystem services. Thus, the expected results aid land-use planners to determine the future trend, location, and size of LULC changes in order to mitigate their damaging consequences.

B. Model Validation

Table X summarizes the area data for the various LULC categories in the actual and modeled LULC maps of the Chalus watershed for the year 2021. As well as, the graph showing the area coverage of LULC types in the actual and simulated maps is illustrated in Fig. 14. To determine the model's correctness, the quality of the simulated LULC map was compared with the actual LULC map. The k-index values that compared the simulated LULC map with the actual LULC map of the year 2021 resulted in a Kstandard = 0.9160, Kno = 0.9379, Klocation = 0.9318, and KlocationStrata = 0.9320. The achieved k-index values are greater than 90 %, showing good agreement between the simulated and actual LULC maps.

Table XI represents statistical agreement information [23] between the actual and modeled LULC maps of the Chalus

TABLE XI
ANALYSIS OF VALIDATION RESULTS

Agreement/Disagreement	Value	Value (%)
Agreement chance	0.1111	11.11
Agreement quantity	0.2321	23.21
Agreement GridCell	0.6016	60.16
Disagreement GridCell	0.0440	4.40
Disagreement quantity	0.0112	1.12

watershed. Quantity disagreement indicates that cell quantity of the same LULC category of the simulated map differs from the actual map. GridCell disagreement occurs when cell's location [9] of the same LULC type of the simulated map differs from the actual map. In this research, the value of disagreement quantity (0.0112) is lower than disagreement GridCell (0.0440), which shows the model is more capable to forecast the LULC changes in quantity than in location. The agreement measures represent the overall proportion correct (94.48 %) for SVM-MC model.

IV. CONCLUSION

The purpose of this research was to detect changes in the LULC map of the Chalus watershed during the last two decades using multitemporal Landsat data and to forecast the LULC map for the study region in 2040 using the SVM-MC model. Using a segmentation classification procedure by combining two pixel-based classifiers (decision forest and fuzzy ARTMAP) with segment-based classification, eight major LULC classes were identified where, in general, grassland is the main LULC class of the watershed that covered 33.64 % of the area in 2021. During 2001–2021, the significant increase of agricultural land (14317 ha) and barren area (9063 ha), and the sharp decline of grassland (26215 ha) and forest cover (5989 ha) were the major LULC changes in the Chalus watershed. Afterward, the simulated LULC map of 2021 was produced by using 2001 and 2014 classified maps to compare with the actual LULC map of 2021 for model validation. Then, the transition potential maps and the transition probability matrix for the year 2040 were provided by the SVM algorithm and the Markov chain model, respectively, to predict the LULC map for 2040. The predicted results showed a considerable decrease in grassland from 33.64 % (57915.52 ha) in 2021 to 27.72 % of area (47717.36 ha) in 2040 with a significant increase in agricultural land from 11.072 % to 16.30 % of area and barren area from 9.49 % to 12.86 % of area during 2021–2040. In addition, forest cover will continue to decrease from 29.46 % (50720.2667 ha) in 2021 to 25.67 % of area (44207.78694 ha) in 2040. Therefore, understanding the spatiotemporal changes of LULC types is extremely important in sustainable land management, monitoring natural disasters, and natural resource assessment.

REFERENCES

[1] M. F. Baig, M. R. U. Mustafa, I. Baig, H. B. Takaijudin, and M. T. Zeshan, "Assessment of land use land cover changes and future predictions using CA-ANN simulation for Selangor, Malaysia," *Water*, vol. 14, no. 3, 2022, Art. no. 402.

[2] M. T. Zeshan, M. R. U. Mustafa, and M. F. Baig, "Article monitoring land use changes and their future prospects using GIS and ANN-CA for Perak River Basin, Malaysia," *Water (Switzerland)*, vol. 13, Art. no. 2286, 2021.

[3] S. Talukdar *et al.*, "Land-use land-cover classification by machine learning classifiers for satellite observations—A review," *Remote Sens.*, vol. 12, 2020, Art. no. 1135.

[4] IPCC, "IPCC SR: Climate change and land," *An IPCC Spec. Rep. Clim. Chang. Desertif. L. Degrad. Sustain. L. Manag. Food Secur. Greenh. gas fluxes Terr. Ecosyst.*, 2019.

[5] W. Y. Lam, J. Chatterton, S. Sim, M. Kulak, A. M. Beltran, and M. A. J. Huijbregts, "Estimating greenhouse gas emissions from direct land use change due to crop production in multiple countries," *Sci. Total Environ.*, vol. 755, 2021, Art. no. 143338.

[6] P. M. Fearnside, W. F. Laurance, S. E. Applications, N. Aug, and W. E. Laurance, "Tropical deforestation and greenhouse-gas emissions," *Environ. Res. Lett.*, vol. 2, 2012, Art. no. 045021.

[7] J. Ngondo, J. Mango, R. Liu, J. Nobert, A. Dubi, and H. Cheng, "Land-use and land-cover (LULC) change detection and the implications for coastal water resource management in the Wami–Ruvu basin, Tanzania," *Sustainability*, vol. 13, 2021, Art. no. 4092.

[8] A. Oljirra, "The causes, consequences and remedies of deforestation in Ethiopia," *J. Degraded Mining Lands Manage.*, vol. 6, pp. 1747–1754, 2019.

[9] S. W. Wang, L. Munkhnasan, and W. K. Lee, "Land use and land cover change detection and prediction in Bhutan's high altitude city of Thimphu, using cellular automata and Markov chain," *Environ. Challenges*, vol. 2, 2021, Art. no. 100017.

[10] A. Sharifi, "Flood mapping using relevance vector machine and SAR data: A case study from Aqqala, Iran," *J. Indian Soc. Remote Sens.*, vol. 48, no. 9, pp. 1289–1296, 2020.

[11] P. Hu *et al.*, "Evaluation of vegetation indices and phenological metrics using time-series MODIS data for monitoring vegetation change in Punjab, Pakistan," *Water (Switzerland)*, vol. 13, 2021, Art. no. 2550.

[12] S. Felegari *et al.*, "Integration of sentinel 1 and sentinel 2 satellite images for crop mapping," *Appl. Sci.*, vol. 11, no. 21, 2021, Art. no. 10104.

[13] S. Ghaderizadeh, D. Abbasi-Moghadam, A. Sharifi, N. Zhao, and A. Tariq, "Hyperspectral image classification using a hybrid 3D-2D convolutional neural networks," *IEEE J. Sel. Topics Appl. Earth Observ. Remote Sens.*, vol. 14, pp. 7570–7588, 2021, doi: 10.1109/JSTARS.2021.3099118.

[14] A. Tariq *et al.*, "Spatio-temporal analysis of forest fire events in the Margalla Hills, Islamabad, Pakistan using socio-economic and environmental variable data with machine learning methods," *J. Forest Res.*, vol. 33, no. 1, pp. 183–194, 2022.

[15] A. Sharifi and J. Amini, "Speckle reduction of PolSAR images in forest regions using fast ICA algorithm," *J. Indian Soc. Remote Sens.*, vol. 13, pp. 339–346, 2015.

[16] A. Kosari, A. Sharifi, A. Ahmadi, and M. Khoshsima, "Remote sensing satellite's attitude control system: Rapid performance sizing for passive scan imaging mode," *Aircr. Eng. Aerosp. Technol.*, vol. 92, no. 7, pp. 1073–1083, 2020.

[17] A. Sharifi, "Estimation of biophysical parameters in wheat crops in Golestan province using ultra-high resolution images," *Remote Sens. Lett.*, vol. 9, no. 6, pp. 559–568, 2018.

[18] R. Girma, C. Fürst, and A. Moges, "Land use land cover change modeling by integrating artificial neural network with cellular Automata-Markov chain model in Gidabo river basin, main Ethiopian rift," *Environ. Challenges*, vol. 6, 2022, Art. no. 100419.

[19] P. Sobhani, H. Esmaeilzadeh, and H. Mostafavi, "Simulation and impact assessment of future land use and land cover changes in two protected areas in Tehran, Iran," *Sustain. Cities Soc.*, vol. 75, 2021, Art. no. 103296.

[20] K. Jafarpour Ghalehteimouri, A. Shamsoddini, M. N. Mousavi, F. Binti Che Ros, and A. Khedmatzadeh, "Predicting spatial and decadal of land use and land cover change using integrated cellular automata Markov chain model based scenarios (2019–2049) Zarriné-Rūd river basin in Iran," *Environ. Challenges*, vol. 6, 2022, Art. no. 100399.

[21] E. Gidey, O. Dikinya, R. Sebego, E. Segosebe, and A. Zenebe, "Cellular automata and Markov chain (CA_Markov) model-based predictions of future land use and land cover scenarios (2015–2033) in Raya, Northern Ethiopia," *Model. Earth Syst. Environ.*, vol. 3, pp. 1245–1262, 2017.

[22] H. Sha, L. Tang, J. P. Hupy, Y. Wang, G. Shao, and S. Kumar, "A commentary review on the use of normalized difference vegetation index (NDVI) in the era of popular remote sensing," *J. Forestry Res.*, vol. 32, pp. 1–6, 2021, doi: 10.1007/s11676-020-01155-1.
[23] S. U. Din and H. W. L. Mak, "Retrieval of land-use/land cover change (LUCC) maps and urban expansion dynamics of Hyderabad, Pakistan via Landsat datasets and support vector machine framework," *Remote Sens.*, vol. 13, 2021, Art. no. 3337.
[24] C. Liu, W. Li, G. Zhu, H. Zhou, H. Yan, and P. Xue, "Land use/land cover changes and their driving factors in the northeastern Tibetan plateau based on geographical detectors and Google Earth engine: A case study in Gannan prefecture," *Remote Sens.*, vol. 12, 2020, Art. no. 3139.
[25] S. W. Wang, B. M. Gebru, M. Lamchin, R. B. Kayastha, and W. K. Lee, "Land use and land cover change detection and prediction in the Kathmandu district of Nepal using remote sensing and GIS," *Sustainability*, vol. 12, 2020, Art. no. 3925.
[26] T. Belay and D. A. Mengistu, "Impacts of land use/land cover and climate changes on soil erosion in Muga watershed, upper blue Nile basin (ABAY), Ethiopia," *Ecol. Process.*, vol. 10, 2021, Art. no. 68.
[27] M. K. Leta, T. A. Demissie, and J. Tränckner, "Modeling and prediction of land use land cover change dynamics based on land change modeler (LCM) in Nashe watershed, upper blue Nile basin, Ethiopia," *Sustainability*, vol. 13, 2021, Art. no. 3740.
[28] D. Abijith and S. Saravanan, "Assessment of land use and land cover change detection and prediction using remote sensing and CA Markov in the northern coastal districts of Tamil Nadu, India," *Environ. Sci. Pollut. Res.*, 2021.
[29] H. Zhai *et al.*, "Understanding spatio-temporal patterns of land use/land cover change under urbanization in Wuhan, China, 2000–2019," *Remote Sens.*, vol. 13, 2021, Art. no. 3331.
[30] E. Alcaras, C. Parente, and A. Vallario, "The importance of the coordinate transformation process in using heterogeneous data in coastal and marine geographic information system," *J. Mar. Sci. Eng.*, vol. 8, 2020, Art. no. 708.
[31] G. Sarp, "Spectral and spatial quality analysis of pan-sharpening algorithms: A case study in Istanbul," *Eur. J. Remote Sens.*, vol. 47, pp. 19–28, 2014.
[32] Y. Anteneh, T. Stellmacher, G. Zeleke, W. Mekuria, and E. Gebremariam, "Dynamics of land change: Insights from a three-level intensity analysis of the Legedadie-dire catchments, Ethiopia," *Environ. Monit. Assess.*, vol. 190, 2018, Art. no. 390.
[33] T. Adugna, W. Xu, and J. Fan, "Comparison of random forest and support vector machine classifiers for regional land cover mapping using coarse resolution FY-3C images," *Remote Sens.*, vol. 14, no. 3, 2022, Art. no. 574.
[34] B. Mannan, J. Roy, and A. K. Ray, "Fuzzy ARTMAP supervised classification of multi-spectral remotely-sensed images," *Int. J. Remote Sens.*, vol. 19, pp. 776–774, 1998.
[35] M. Zabihi, H. Moradi, M. Gholamalifard, A. K. Darvishan, and C. Fürst, "Landscape management through change processes monitoring in Iran," *Sustainability*, vol. 12, 2020, Art. no. 1753.
[36] S. Hasan, W. Shi, X. Zhu, S. Abbas, and H. U. A. Khan, "Future simulation of land use changes in rapidly urbanizing South China based on land change modeler and remote sensing data," *Sustainability*, vol. 12, 2020, Art. no. 1350.
[37] B. Matlhodi, P. K. Kenabatho, B. P. Parida, and J. G. Maphanyane, "Analysis of the future land use land cover changes in the Gaborone dam catchment using CA-Markov model: Implications on water resources," *Remote Sens.*, vol. 13, 2021, Art. no. 2427.
[38] A. Pérez-Vega, J. F. Mas, and A. Ligmann-Zielinska, "Comparing two approaches to land use/cover change modeling and their implications for the assessment of biodiversity loss in a deciduous tropical forest," *Environ. Model. Softw.*, vol. 29, pp. 11–23, 2012.
[39] K. Islam, M. F. Rahman, and M. Jashimuddin, "Modeling land use change using cellular automata and artificial neural network: The case of Chunati wildlife sanctuary, Bangladesh," *Ecol. Indicators*, vol. 88, pp. 439–453, 2018.
[40] R. J. Eastman, *IDRISI TerrSet Tutorial*. Worcester, MA: Clark University, 2015. [Online]. Available: https://clarklabs.org/download/terrset-service-update/
[41] Y. Megahed, P. Cabral, J. Silva, and M. Caetano, "Land cover mapping analysis and urban growth modelling using remote sensing techniques in greater Cairo region-Egypt," *ISPRS Int. J. Geo-Inf.*, vol. 4, 2015, pp. 1750–1769.

Sepideh Jalayer was born in Daregaz, Iran, in 1995. She received the M.Sc. degree in remote sensing engineering from Shahid Rajaee Teacher Training University, Tehran, Iran, in 2022.

Her research interests include geomatics, satellite image processing, and land use/land cover mapping.

Alireza Sharifi was born in Tehran, Iran, in 1981. He received the M.Sc. and Ph.D. degrees in remote sensing engineering from the University of Tehran, Tehran, Iran, in 2008 and 2015, respectively.

He is currently an Assistant Professor of Remote Sensing with the Faculty of Civil Engineering, Shahid Rajaee Teacher Training University, Tehran, Iran. In particular, he is involved in GEOAI program for food security and environmental monitoring.

Dariush Abbasi-Moghadam received the B.S. degree in electrical engineering from Shahid Bahonar University, Kerman, Iran, in 1998, and the M.S. and Ph.D. degrees in electrical engineering from Iran University of Science and Technology, Tehran, Iran, in 2001 and 2011, respectively.

He was primarily with the Advanced Electronic Research Center—Iran from 2001– 2003 and worked on the design and analysis of satellite communication systems. In September 2004, he joined Iranian Telecommunications Company, Tehran, as a Research Engineer. He is currently with the Department of Electrical Engineering, Shahid Bahonar University of Kerman, Kerman, Iran, as an Associate Professor. His research interests include in the area of wireless communications, satellite communication systems, remote sensing, and signal processing.

Aqil Tariq was born in Rawalpindi, Pakistan. He received the Ph.D. degree in photogrammetry and remote sensing from the State Key Laboratory of Information Engineering in Surveying, Mapping, and Remote Sensing (LIESMARS), Wuhan University, Wuhan, China, in 2021.

He is currently working with LIESMARS, Wuhan University. His research interests area are 3-D geoinformation, urban analytics, spatial analysis to examine land use/land cover, geospatial data science, agriculture monitoring, forest fire, forest monitoring, forest cover dynamics, spatial statistics, multicriteria algorithms, ecosystem sustainability, hazards risk reduction, statistical analysis and modeling using Python, R, and MATLAB.

Shujing Qin received the Ph.D. degree in agricultural water-soil engineering from China Agricultural University, Beijing, China, in 2020.

She is currently with the State Key Laboratory of Water Resources and Hydropower Engineering Science, Wuhan University, Wuhan, China. Her research interests include flux measurement and modeling of terrestrial ecosystem, eco-hydrology, land-atmosphere interaction, and climate change.